# Combining maximum-entropy and the Mexican hat wavelet to reconstruct the microwave sky

P. Vielva,[1,2]★ R. B. Barreiro,[3] M. P. Hobson,[3] E. Martínez-González,[1] A. N. Lasenby,[3] J. L. Sanz[1] and L. Toffolatti[4]

[1]*Instituto de Física de Cantabria (CSIC – UC), Fac. Ciencias, Avda. de los Castros s/n, 39005 Santander, Spain*
[2]*Departamento de Física Moderna, Universidad de Cantabria, Avda. de los Castros s/n, 39005 Santander, Spain*
[3]*Astrophysics Group, Cavendish Laboratory, Madingley Road, Cambridge CB3 0HE*
[4]*Departamento de Física, Universidad de Oviedo, c/Calvo Sotelo s/n, 33007 Oviedo, Spain*

**ABSTRACT**

We present a maximum-entropy method (MEM) and 'Mexican hat' wavelet (MHW) joint analysis to recover the different components of the microwave sky from simulated observations by the ESA *Planck Surveyor* satellite in a small patch of the sky ($12.8 \times 12.8 \text{ deg}^2$). This combined method allows one to improve the CMB, Sunyaev–Zel'dovich and Galactic foregrounds separation achieved by the MEM technique alone. In particular, the reconstructed CMB map is free from any bright point-source contamination. The joint analysis also produces point-source catalogues at each *Planck* frequency that are more complete and accurate than those obtained by either method on its own. The results are especially improved at high frequencies where infrared galaxies dominate the point-source contribution. Although this joint technique has been performed on simulated *Planck* data, it could easily be applied to other multifrequency CMB experiments, such as the forthcoming NASA *MAP* satellite or the recently-performed BOOMERANG and MAXIMA experiments.

**Key words:** methods: data analysis – techniques: image processing – cosmic microwave background.

## 1 INTRODUCTION

The cosmic microwave background (CMB) is one of the most powerful observational tools for understanding our Universe. Indeed, an accurate knowledge of CMB anisotropies can place tight constraints on fundamental parameters such as the amount of matter in the Universe and its overall geometry. Observations of the CMB also allow one to discriminate between different models of structure formation.

Recent CMB experiments such as BOOMERANG (de Bernardis et al. 2000) and MAXIMA (Balbi et al. 2000) have set strong constraints on the geometry of the Universe, showing that it is close to spatially flat. Nevertheless, there remain numerous unbroken degeneracies in the full set of parameters that define the currently favoured inflationary cold dark matter (CDM) cosmological model. In order to resolve these degeneracies, a new generation of CMB satellite experiments is currently in preparation, most notably the NASA *MAP* mission (Bennet et al. 1996) and the ESA *Planck Surveyor* (Mandolesi et al. 1998; Puget et al. 1998). These experiments will provide high-resolution all-sky maps of the CMB

anisotropies, which will allow a highly accurate estimation of a large set of cosmological parameters.

An important issue for CMB satellite missions is the separation of foreground emission from the CMB signal. An accurate means of performing this separation is vital in order to make full use of the high-resolution CMB maps these experiments will produce. The main foregrounds to be separated from the CMB signal are those due to our own Galaxy (dust, free–free and synchrotron emission) and extragalactic emission due, principally, to the Sunyaev–Zel'dovich effect (both thermal and kinetic) and point sources.

A preliminary application of neural-network techniques in this field has recently been performed with promising results (Baccigalupi et al. 2000), but this approach is not at present sufficiently sophisticated to accommodate multifrequency data arising from convolutions with beams of different size and subject to different levels of instrumental noise. Nevertheless, more traditional techniques based on the maximum-entropy method (MEM) have been shown to provide an efficient and accurate way of performing the component separation (Hobson et al. 1998, hereinafter H98).

As one might expect, the MEM technique is particularly successful at using multifrequency data to identify foreground

★E-mail: vielva@ifca.unican.es

emission from physical components whose spectral signatures are (reasonably) well known. It is therefore not surprising that the most problematic foreground to remove is that due to extragalactic point sources. These differ from the other components in the important respect that the spectral behaviour of point sources differs from one source to the next and, moreover, is notoriously difficult to predict. We can, however, make some headway by at least identifying the likely populations of point sources at different observing frequencies. Our knowledge of point-source populations is increasing with new observations, but there are still great uncertainties. In the absence of extensive observations at microwave frequencies, the currently-favoured approach is to use the Toffolatti et al. (1998) model, which provides an estimate of point-source populations based on existing observations and basic physical mechanisms. This model can be used to generate simulated point-source emission at different observing frequencies. From 30 to 100 GHz, the main point-source emission is due to radio selected flat-spectrum AGNs (radio-loud quasars, blazars, etc.). From 300 to 900 GHz, infrared selected sources – starburst and late-type galaxies at intermediate-to-low redshift and high-redshift ellipticals – account for most point-source emission. At intermediate frequencies, both populations contribute approximately equally.

The problem of removing emission due to point sources from CMB observations has been addressed by several authors. For example, Tegmark & Oliveira-Costa (1998, hereinafter TOC98) suggest a straightforward harmonic filter technique that is optimized to detect and subtract point sources, whereas Hobson et al. (1999, hereinafter H99) propose treating point-source emission as an additional generalized 'noise' contribution within the framework of the MEM approach discussed in H98. Tenorio et al. (1999) present a wavelet technique to subtract point sources, but the wavelet basis used in this work is not the optimal one for this purpose. This point is addressed in Sanz, Herranz & Martínez-González (2000), where it is shown that the 'Mexican hat' wavelet (MHW) is in fact optimal for detecting point sources under reasonable conditions, the most important assumption being that the beam is well approximated by a Gaussian.

The application of this wavelet to realistic simulations has been presented in Cayón et al. (2000, hereinafter C00) and extended in Vielva et al. (2001, hereinafter V01). The main advantage of the MHW method over the previous work is that the algorithm does not require any assumptions to be made regarding the statistical properties of the point-source population or the underlying emission from the CMB (or other foreground components).

The aim of this paper is to show how the MEM and MHW approaches are in fact complementary and can be combined to improve the accuracy of the separation of diffuse foregrounds from the CMB and increase the number of points sources that are identified and successfully subtracted. The technique proposed in this paper is as follows. First, we apply the MHW to the multifrequency simulated *Planck* maps to detect the brightest point sources at each observing frequency, which are subtracted from the original data. The MEM algorithm is then applied to these processed maps in order to recover the rest of the components of the microwave sky. These reconstructed components are then used as inputs to produce 'mock' data and subtracted from the original data maps. Since we expect our reconstructions to be reasonably accurate, the residuals maps obtained in this way would mostly contain noise and the contribution from point sources. Finally, we apply the MHW on these residuals maps in order to recover a more complete and accurate point-source catalogue.

In this paper the combined method is applied to simulated

observation by the *Planck* satellite, but the technique could easily be applied to *MAP* data or to existing multifrequency observations by the BOOMERANG or MAXIMA balloon experiments. The paper is organized as follows. In the next section we present a brief overview of the MEM and MHW techniques, outlining in particular the advantages and shortcomings of each approach. We then explain why the two approaches can be successfully combined to produce a more powerful joint analysis scheme. In Section 3 we summarize how the simulated *Planck* observations were performed. In Section 4 we present the results of a component separation based on the new joint analysis method, and discuss the improved accuracy of the reconstructions of the diffuse components. In Section 5 we concentrate on the recovery of the point sources themselves and discuss the construction of point-source catalogues from *Planck* observations. Finally, our conclusions are presented in Section 6.

## 2 THE MEM AND MHW TECHNIQUES

In this section, we briefly review the MEM and MHW techniques. A complete description of the MEM component separation algorithm can be found in H98. In addition, H99 describes how to include point sources into the MEM formalism. We therefore provide only a basic outline of the approach. The MHW method is introduced in C00 and extended in V01, and so again we give only a basic summary.

### 2.1 The maximum-entropy method

If we observe the microwave sky in a given direction $x$ at $n_f$ different frequencies, we obtain an $n_f$-component data vector that contains, for each frequency, the temperature fluctuations convolved with the beam in this direction plus instrumental noise. The $\nu$th component of the data vector in the direction $x$ may be written as

$$d_\nu(x) = \int B_\nu(|x - x'|) \sum_{p=1}^{n_c} \mathbf{F}_{\nu p} s_p(x') \, \mathrm{d}^2 x' + \xi_\nu(x) + \epsilon_\nu(x). \qquad (1)$$

In this expression we distinguish between the contributions from the point sources and the $n_c$ physical components for which it is assumed the spectral behaviour is constant and reasonably well-defined (over the observed patch of sky). The latter are collected together in a signal vector with $n_c$ components, such that $s_p(x)$ is the signal from the $p$th physical component at some reference frequency $\nu_0$. The corresponding total emission at the observing frequency $\nu$ is then obtained by multiplying the signal vector by the $n_f \times n_c$ frequency response matrix $\mathbf{F}_{\nu p}$, which includes the spectral behaviour of the considered components as well as the transmission of the $\nu$th frequency channel. This contribution is then convolved with the beam profile $B_\nu(x)$ of the relevant channel. Since the individual spectral dependencies of the point sources are very complicated, we cannot factorize their contribution in this way and so they are added into the formalism as an extra 'noise' term. Thus $\xi_\nu$ is the contribution from point sources, as observed by the instrument at the frequency $\nu$ (hence, convolved with the beam profile). Finally, $\epsilon_\nu$ is the expected level of instrumental noise in the $\nu$th frequency channel and is assumed to be Gaussian and isotropic.

The assumption of a spatially-invariant beam profile in Equation (1) allows us to perform the reconstruction more effectively by working in Fourier space, since we may consider each $k$-mode independently (see H98). Thus, in matrix notation, at each mode

we have

$$d = \mathbf{R}s + \xi + \epsilon = \mathbf{R}s + \zeta, \qquad (2)$$

where $d$, $\xi$ and $\epsilon$ are column vectors each containing $n_f$ complex components and $s$ is a column vector containing $n_c$ complex components. In the second equality we have combined the instrumental noise vector $\epsilon$ and the point-source contribution $\xi$ into a single 'noise' vector $\zeta$. The response matrix $\mathbf{R}$ has dimensions $n_f \times n_c$ and its elements are given by $R_{\nu p}(k) = \breve{B}_\nu(k)\mathbf{F}_{\nu p}$. The aim of any component separation/reconstruction algorithm is to invert Equation (2) in some sense, in order to obtain an estimate $\hat{s}$ of the signal vector at each value of $k$ independently. Owing to the presence of noise, and the fact that the response matrix $\mathbf{R}$ is not square and would, in any case, have some small eigenvalues, a direct inversion is not possible, and so some form of regularized inverse must be sought. Typical methods include singular-valued decomposition, Wiener filtering or the maximum-entropy method.

The elements of the signal vector $s$ at each Fourier mode may well be correlated, this correlation being described by the $n_c \times n_c$ signal covariance matrix $\mathbf{C}$ defined by

$$\mathbf{C}(k) = \langle s(k)s^\dagger(k)\rangle, \qquad (3)$$

where the dagger denotes the Hermitian conjugate. Moreover, if prior information is available concerning these correlations, we would wish to include it in our analysis. We therefore introduce the vector of 'hidden' variables $h$, related to the signal vector by

$$s = \mathbf{L}h, \qquad (4)$$

where the $n_c \times n_c$ lower triangular matrix $\mathbf{L}$ is obtained by performing a Cholesky decomposition of the signal covariance matrix $\mathbf{C} = \mathbf{L}\mathbf{L}^\mathrm{T}$. The reconstruction is then performed entirely in terms of $h$ and the corresponding reconstructed signal vector is subsequently found using Equation (4).

Using Bayes's theorem, we choose our estimator $\hat{h}$ of the hidden vector to be that which maximizes the posterior probability given by

$$\Pr(h|d) \propto \Pr(d|h)\Pr(h), \qquad (5)$$

where $\Pr(d|h)$ is the likelihood of obtaining the data given a particular hidden vector and $\Pr(h)$ is the prior probability that codifies our expectations about the hidden vector before acquiring any data.

As explained in H99, the form of the likelihood function in Equation (5) is given by

$$\Pr(d|h) \propto \exp(-\zeta\dagger\mathbf{N}^{-1}\zeta) \propto \exp[-(d - \mathbf{R}\mathbf{L}h)\dagger\mathbf{N}^{-1}(d - \mathbf{R}\mathbf{L}h)], \qquad (6)$$

where in the last line we have used Equation (2). The noise covariance matrix $\mathbf{N}$ has dimensions $n_f \times n_f$ and at any given $k$-mode is given by

$$\mathbf{N}(k) = \langle \zeta(k)\zeta\dagger(k)\rangle. \qquad (7)$$

Therefore, at a given Fourier mode, the $\nu$th diagonal element of $\mathbf{N}$ contains the ensembled-averaged power spectrum at that mode of the instrumental noise plus the point-source contribution to the $\nu$th frequency channel. The off-diagonal terms give the cross-correlations between different channels; if the noise is uncorrelated between channels, only the point sources contribute to the off-diagonal elements.

For the prior $\Pr(h)$ in Equation (5), we assume the entropic

form

$$\Pr(h) \propto \exp[\alpha S(h, m)], \qquad (8)$$

where $S(h,m)$ is the cross entropy of the complex vectors $h$ and $m$, where $m$ is a model vector to which $h$ defaults in the absence of data. The form of the cross entropy for complex images and the Bayesian method for fixing the regularizing parameter $\alpha$ are discussed in H98. We note that, in the absence of non-Gaussian signals, the entropic prior Equation (8) tends to the Gaussian prior implicitly assumed by Wiener filter separation algorithms, and so in this case the two methods coincide.

The argument of the exponential in the likelihood function of Equation (6) may be identified as (minus) the standard $\chi^2$ misfit statistic, so we may write $\Pr(d|h) \propto \exp[-\chi^2(h)]$. Substituting this expression, together with that for the prior probability given in Equation (8), into Bayes's theorem, we find that maximizing the posterior probability $\Pr(h|d)$ with respect to $h$ is equivalent to minimizing the function

$$\Phi(h) = \chi^2(h) - \alpha S(h, m).$$

This minimization can be performed using a variable metric minimizer (Press et al. 1994) and requires only a few minutes of CPU time on a Sparc Ultra workstation.

## 2.2 The Mexican hat wavelet method

The MHW technique presented by C00 and V01 for identifying and subtracting point sources operates on individual data maps. Let us consider the two-dimensional data map $d_\nu(x)$ at the frequency $\nu$. If the map contains point sources at positions $b_i$ with fluxes or amplitudes $A_i$, together with contributions from other physical components and instrumental noise, then the data map is given by

$$d_\nu(x) = \xi_\nu(x) + n_\nu(x) = \sum_i A_i B_\nu(x - b_i) + n_\nu(x), \qquad (9)$$

where $B_\nu(x)$ is the beam at the observing frequency $\nu$, and in this case the generalized 'noise' $n_\nu(x)$ is defined as all contributions to the data map aside from the point sources.

For the $i$th point source, we may define a 'detection level'

$$D = \frac{A_i/\Omega}{\sigma_n}, \qquad (10)$$

where $\Omega$ is the area under the beam and $\sigma_n$ is the dispersion of the generalized noise field $n_\nu(x)$. In general, the detection level $D$ will be much less than unity for all but the few brightest sources. This is the usual problem one faces when attempting to identify point sources directly in the data map.

As explained in C00, instead of attempting the identification in real space, one can achieve better results by first transforming to *wavelet space*. For a two-dimensional data map $d_\nu(x)$, we define the continuous isotropic wavelet transform by

$$w_d(R, b) = \int \mathrm{d}^2x \, \frac{1}{R^2} \, \psi\left(\frac{|x - b|}{R}\right) d_\nu(x), \qquad (11)$$

where $w(R,b)$ is the wavelet coefficient associated with the scale $R$ at the point $b$ (where the wavelet is centred). The function $\psi(|x|)$ is the *mother* wavelet, which is assumed to be isotropic and satisfies

**Table 1.** The point-source catalogues obtained using the MHW alone (MHWc), MEM alone (MEMc) and the joint analysis method (M&Mc). For each *Planck* observing frequency, we list the number of sources detected, the flux limit of the catalogue and the average of the absolute value of the percentage error for the amplitude estimation. The numbers in brackets in the second column indicate the number of point sources that are detected by the $5\sigma_{w_d}$ criterion (see text for details).

| Frequency (GHz) | MHWc | | | MEMc | | | M&Mc | | |
|---|---|---|---|---|---|---|---|---|---|
| | Number of detections | Min Flux (Jy) | $\bar{E}$ (per cent) | Number of detections | Min Flux (Jy) | $\bar{E}$ (per cent) | Number of detections | Min Flux (Jy) | $\bar{E}$ (per cent) |
| 30 | 15 (4) | 0.13 | 14.0 | 32 | 0.09 | 14.9 | 30 | 0.09 | 14.0 |
| 44 | 11 (3) | 0.27 | 11.2 | 28 | 0.11 | 14.2 | 28 | 0.11 | 13.2 |
| 70 | 7 (5) | 0.30 | 7.9 | 38 | 0.08 | 11.8 | 35 | 0.09 | 11.4 |
| 100 (LFI) | 12 (3) | 0.23 | 11.8 | 37 | 0.08 | 16.4 | 44 | 0.06 | 18.4 |
| 100 (HFI) | 17 (7) | 0.14 | 14.1 | 72 | 0.04 | 17.3 | 74 | 0.03 | 17.4 |
| 143 | 11 (4) | 0.16 | 18.0 | 0 | – | – | 5 | 0.32 | 12.4 |
| 217 | 15 (5) | 0.08 | 14.4 | 0 | – | – | 5 | 0.25 | 15.4 |
| 353 | 16 (10) | 0.15 | 14.3 | 38 | 0.08 | 28.7 | 37 | 0.08 | 34.9 |
| 545 | 37 (29) | 0.29 | 14.1 | 89 | 0.18 | 26.4 | 121 | 0.15 | 17.2 |
| 857 | 306 (86) | 0.30 | 16.5 | 458 | 0.23 | 20.6 | 492 | 0.19 | 19.5 |

**Table 2.** Basic observational parameters of the 10 frequency channels of the *Planck Surveyor* satellite. Column two lists the fractional banwidths. The FWHM in column three assumes a Gaussian beam. In column four the instrumental noise level is $\Delta T$ (μK) per resolution element for 12 months of observation.

| Frequency (GHz) | Fractional bandwidth ($\Delta\nu/\nu$) | FWHM (arcmin) | $\sigma_{noise}$ (μK) |
|---|---|---|---|
| 30 | 0.20 | 33.0 | 4.4 |
| 44 | 0.20 | 23.0 | 6.5 |
| 70 | 0.20 | 14.0 | 9.8 |
| 100 (LFI) | 0.20 | 10.0 | 11.7 |
| 100 (HFI) | 0.25 | 10.7 | 4.6 |
| 143 | 0.25 | 8.0 | 5.5 |
| 217 | 0.25 | 5.5 | 11.7 |
| 353 | 0.25 | 5.0 | 39.3 |
| 545 | 0.25 | 5.0 | 400.7 |
| 857 | 0.25 | 5.0 | 18182 |

the conditions

$$\int d^2\boldsymbol{x}\,\psi(x) = 0 \qquad \text{(compensation)}$$

$$\int d^2\boldsymbol{x}\,|\psi(x)|^2 = 1 \qquad \text{(normalization)}$$

$$C_\psi = (2\pi)^2 \int_0^\infty dk\, k^{-1}|\tilde{\psi}(k)|^2 < \infty \quad \text{(admissibility)},$$

where $\tilde{\psi}$ denotes the Fourier transform of $\psi$, $x = |\boldsymbol{x}|$ and $k = |\boldsymbol{k}|$. The wavelet coefficients given by Equation (11) characterize the contribution from structure on a scale $R$ to the value of the map at the position $\boldsymbol{b}$.

By analogy with Equation (10), in wavelet space, we define the detection level for the $i$th point source (as a function of scale $R$) by

$$D_w(R) = \frac{w_\xi(R, \boldsymbol{b}_i)}{\sigma_{w_n}(R)}, \qquad (12)$$

where $w_\xi(R,\boldsymbol{b}_i)$ is the wavelet coefficient of the field $\xi_\nu(\boldsymbol{x})$ at the location of the $i$th point source, and $\sigma_{w_n}^2(R)$ is the dispersion of the wavelet coefficients $w_n(R, \boldsymbol{b})$ of the generalized noise field $n_\nu(\boldsymbol{x})$. It

is straightforward to show that

$$\sigma_{w_n}^2(R) = 2\pi \int_{k_{min}}^{k_{max}} dk\, kP(k)|\tilde{\psi}(Rk)|^2, \qquad (13)$$

where $P(k)$ is the power spectrum of $n_\nu(\boldsymbol{x})$. The integral limits, $k_{min}$ and $k_{max}$, correspond to the maximum and minimum scales of the sky patch analysed, i.e. the patch and pixel scales, respectively.

The detection level $D_w(R)$ in wavelet space will have a maximum value at some scale $R = R_0$. This scale is practically the same for all point sources, and may be found by solving $dD_w(R_0)/dR = 0$. In general, the optimal scale is of the order of the beam dispersion $\sigma_a$ (see V01, section 3, for a discussion about how the noise and the coherence scale of the background determine the optimal scale). In order that the wavelet coefficients are optimally sensitive to the presence of the point source, we must make the value of $D_w(R_0)$ as large as possible. This is achieved through an appropriate choice both of the mother wavelet $\psi(x)$ and the optimal scale. If the beam profile is Gaussian and the power spectrum of the generalized noise field is scale-free, Sanz et al. (2000) show that, for a wide range of spectral indices of the power spectrum, the Mexican hat wavelet is optimal. The two-dimensional MHW is given by

$$\psi(x) = \frac{1}{\sqrt{2\pi}}\left[2 - \left(\frac{x}{R}\right)^2\right]e^{-x^2/2R^2}, \qquad (14)$$

from which we find

$$w_\xi(R, \boldsymbol{b}_i) = 2\sqrt{2\pi}\frac{A_i}{\Omega}\frac{(R/\sigma_a)^2}{(1 + (R/\sigma_a)^2)^2}, \qquad (15)$$

where $A_i$ is the amplitude of the $i$th point source, $\Omega$ is the area under the Gaussian beam and $\sigma_a$ is the beam dispersion. In Equation (15) it is assumed that any overlap of the (convolved) point sources is negligible. That is a good approximation for the brightest point sources, the ones that the MHW is able to detect. In fact, the number of point sources detected at each frequency (see Table 1) corresponds only to a small percentage of the number of resolution elements (see Table 2) contained at each *Planck* frequency channel (~6 per cent at 30 GHz, the most unfavourable case). Therefore, the probability of finding two or more bright point sources inside the same resolution element is very low. The advantage of identifying point sources in wavelet space rather than
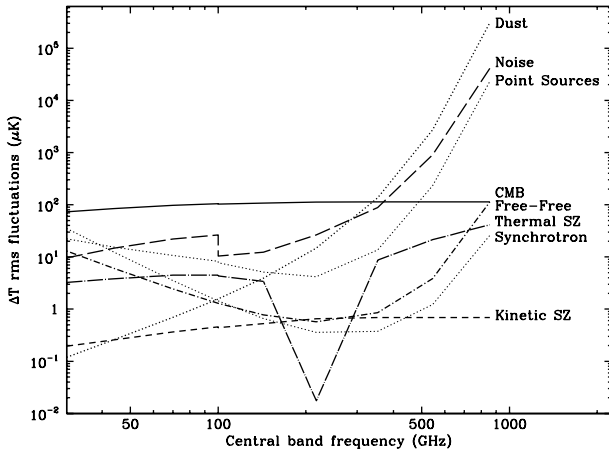
**Figure 1.** The $12.8 \times 12.8$ deg$^2$ realizations of the six input components used to produce the simulated *Planck* data. They include contributions from the CMB, the thermal and kinematic Sunyaev–Zel'dovich (SZ) effects, extragalactic point sources, and Galactic thermal dust, free–free and synchrotron emission. Each component is plotted at 300 GHz and has been convolved with a Gaussian beam of FWHM 5 arcmin (the highest resolution expected for the *Planck* satellite). The map units are equivalent thermodynamic temperature in μK.

real space may then be characterized by the amplification factor

$$\mathcal{A} = \frac{D_w(R_0)}{D} = 2\sqrt{2\pi}\,\frac{(R_0/\sigma_a)^2}{(1 + (R_0/\sigma_a)^2)^2}\,\frac{\sigma_n}{\sigma_{w_n}(R_0)}. \tag{16}$$

In practice, it is clear that we do not have access to the wavelet coefficients of the fields $\xi_\nu(\boldsymbol{x})$ and $n_\nu(\boldsymbol{x})$ separately, but only to the wavelet coefficients of the total data map $d_\nu(\boldsymbol{x}) = \xi_\nu(\boldsymbol{x}) + n_\nu(\boldsymbol{x})$. Nevertheless, if the detection level $D_w(R)$ for the $i$th point source is reasonably large, we would expect $w_\xi(R, \boldsymbol{b}_i) \approx w_d(R, \boldsymbol{b}_i)$. Also, if we assume that the power spectrum of the point-source emission is negligible as compared with that of the generalized noise field, then $\sigma_{w_n}(R) \approx \sigma_{w_d}(R)$. Thus our algorithm for detecting point sources is as follows. Using the above approximations, we first calculate the optimal scale $R_0$. We then calculate the wavelet transform $w_d(R_0, \boldsymbol{b})$ of the data map at the optimal scale. The wavelet coefficients are then analysed to find sets of connected pixels above a certain threshold $\sigma_{w_d}(R_0)$. The maxima of these spots are taken to correspond to the locations of the point sources.

For every point source detected in the above way, we then go on to estimate its flux. This is achieved by performing a multiscale fit as follows. For each point-source location $\boldsymbol{b}_i$, the wavelet transform $w_d(R, \boldsymbol{b}_i)$ is calculated at a number of scales $R$ and compared with the theoretical curve Equation (15). This comparison is performed by calculating the standard misfit statistic

$$\chi^2 = [\boldsymbol{w}^{(\mathrm{exp})} - \boldsymbol{w}^{(\mathrm{theo})}]^{\mathrm{T}}\mathbf{V}^{-1}[\boldsymbol{w}^{(\mathrm{exp})} - \boldsymbol{w}^{(\mathrm{theo})}], \tag{17}$$

where the $k$th element of the vector $\boldsymbol{w}^{(\mathrm{exp})}$ is $w_d^{(\mathrm{exp})}(R_k, \boldsymbol{b}_i)$ (and similarly for the vector of theoretical wavelet coefficients). The matrix $\mathbf{V}$ is the empirical covariance matrix of the wavelet coefficients on different scales, which is given by

$$V_{jk} = \langle w_d^{(\mathrm{exp})}(R_j, \boldsymbol{b})w_d^{(\mathrm{exp})}(R_k, \boldsymbol{b})\rangle, \tag{18}$$

where the average is over position $\boldsymbol{b}$.

### 2.3 MEM and MHW joint analysis

In H99, the MEM technique is shown to be effective at performing

a full component separation in the presence of point sources. In particular, the reconstructed maps of the separate diffuse components contain far less point-source contamination than the input data maps. Moreover, by comparing the true data maps with simulated data maps produced from the separated components, it is possible to obtain point-source catalogues at each observing frequency. Nevertheless, the MEM approach does have its limitations. Since the point sources are modelled as an additional generalized noise component, it is not surprising that MEM performs well in identifying and removing the large number of point sources with low-to-intermediate fluxes. However, it is rather poorer at removing the contributions from the brightest point sources. These tend to remain in the reconstructed maps of the separate diffuse components, although with much reduced amplitudes.

The MHW technique, on the other hand, performs best when identifying and removing the brightest point sources. Indeed, in detecting bright sources the MHW technique generally out-performs other techniques such as SExtractor (Bertin & Arnouts 1996) and standard harmonic filtering (TOC98). Moreover, the amplitudes of the bright sources are also accurately estimated. For weaker sources, however, the MHW technique performs more poorly by either inaccurately estimating the flux or failing to detect the source altogether.

The strengths and weaknesses of the MEM and MHW approaches clearly indicate that they are complementary techniques, and that a combined approach might lead to improved results as compared with using each method independently. We thus propose the following method for analysing multifrequency observations of the CMB that contain point-source contamination. First, the data map at each observing frequency is analysed separately using the MHW in order to detect and remove as many bright point sources as possible and obtain accurate estimates of their fluxes. The processed data maps are then taken as the inputs to the generalized MEM approach discussed in H99. As we will demonstrate in Section 4, the MEM analysis of these processed maps leads to more accurate reconstructed maps of the separate diffuse components. This leads in turn to more accurate residual maps between the true input data with the data simulated from the reconstructions. These residual maps are then analysed with the MHW in order both to refine the original estimates of the fluxes of the bright point sources and to detect fainter sources. Thus, the joint analysis not only gives a more complete point-source catalogue, but also improves the quality of the reconstructed maps of the CMB and other foreground components.

## 3 SIMULATED OBSERVATIONS

As mentioned in the introduction, the joint analysis technique can be applied to any multifrequency observations of the CMB that may contain point-source emission. Thus, for example, the method could straightforwardly be applied to the existing BOOMERANG or MAXIMA data sets, or to observations by the forthcoming NASA *MAP* satellite. Nevertheless, in order to test the capabilities of the joint analysis method to the fullest extent, in this paper we apply it to simulated observations by the proposed ESA *Planck Surveyor* satellite. The basic observational parameters of the *Planck* mission instruments (HFI and LFI) are listed in Table 2.

The simulated data are similar to those used in H99. They include contributions from the primordial CMB, the thermal and kinetic Sunyaev–Zel'dovich effects, extragalactic point sources, Galactic thermal dust and free–free and synchrotron emission.
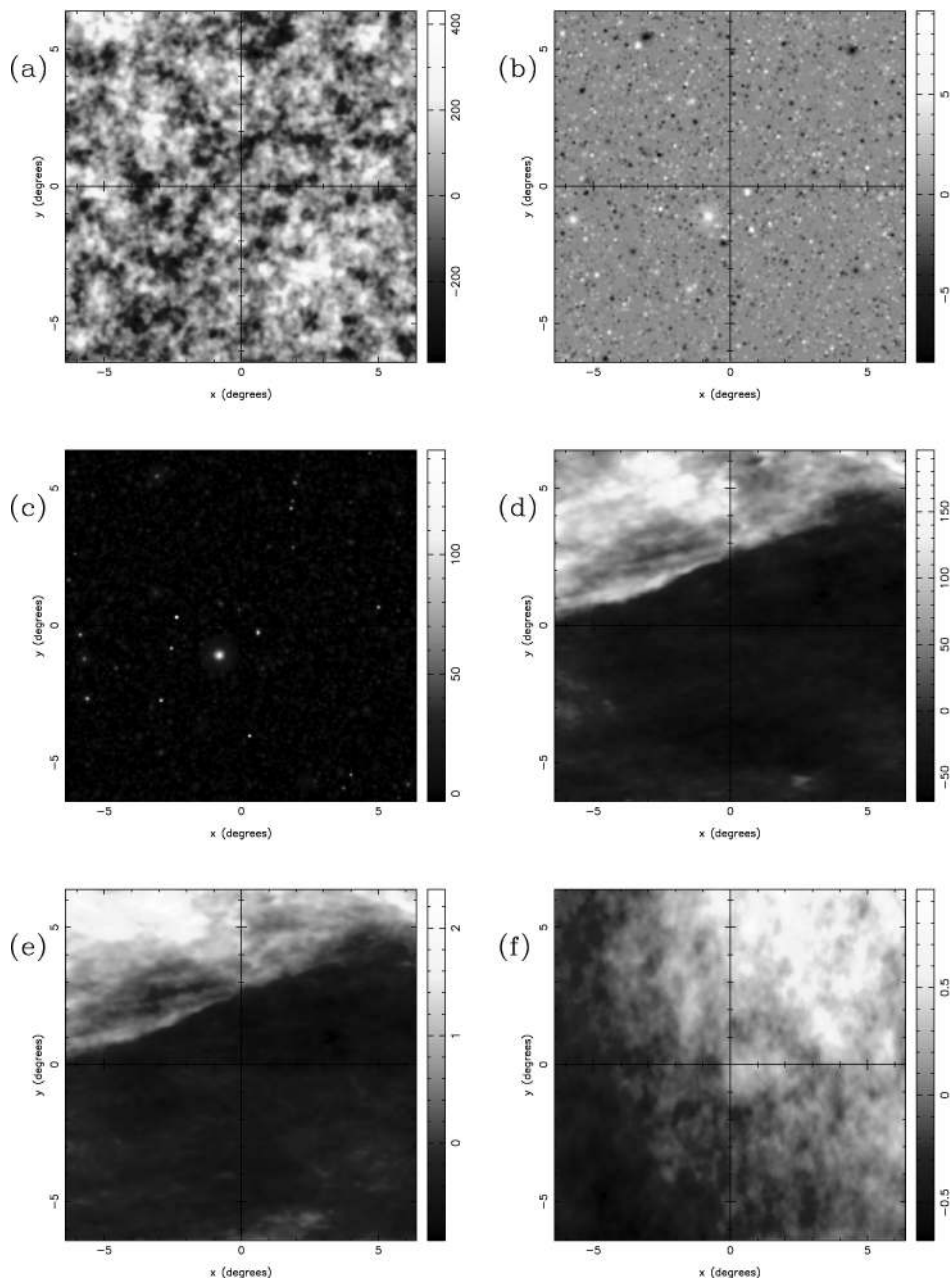
**Figure 2.** The rms thermodynamic temperature fluctuations at the *Planck* observing frequencies due to each physical component, after convolution with the appropriate beam and assuming a sampling rate of FWHM/2.4. The rms instrumental noise per pixel at each frequency is also plotted.

Aside from the point sources, we assume that the emission of each physical component can be factorized into a spatial template at 300 GHz with a known frequency dependence. In Fig. 1 we have plotted the six component templates at 300 GHz. Each map covers a $12.8 \times 12.8$-deg$^2$ patch of sky and has been convolved with a Gaussian beam with FWHM 5 arcmin (i.e. the highest *Planck* resolution).

The CMB map is a Gaussian realization of a spatially-flat inflationary/CDM model with $\Omega_m = 0.3$ and $\Omega_\Lambda = 0.7$, for which the $C_\ell$ coefficients were generated using CMBFAST (Seljak & Zaldarriaga 1996). The thermal Sunyaev–Zel'dovich map is taken from the simulations of Diego et al. (2001) and assume the same cosmological model as that used for the CMB. The kinetic SZ field is produced by assuming that the line-of-sight cluster velocities are drawn from a Gaussian distribution with zero mean and rms

400 km s$^{-1}$. The extragalactic point-source simulations adopt the model of Toffolatti et al. (1998) and also assume the same cosmological model.

The Galactic thermal dust emission is created using the template of Finkbeiner, Davis & Schlegel (1999). The frequency dependence of the dust emission is assumed to follow a grey-body function characterized by a dust temperature of 18 K and an emissivity $\beta = 2$. The distribution of Galactic free–free emission is poorly known. Current experiments such as the H-$\alpha$ Sky Survey[1] and the WHAM project[2] should soon provide maps of $H_\alpha$ emission that could be used as templates. For the time being, however, we create a free–free template that is correlated with the dust emission

---
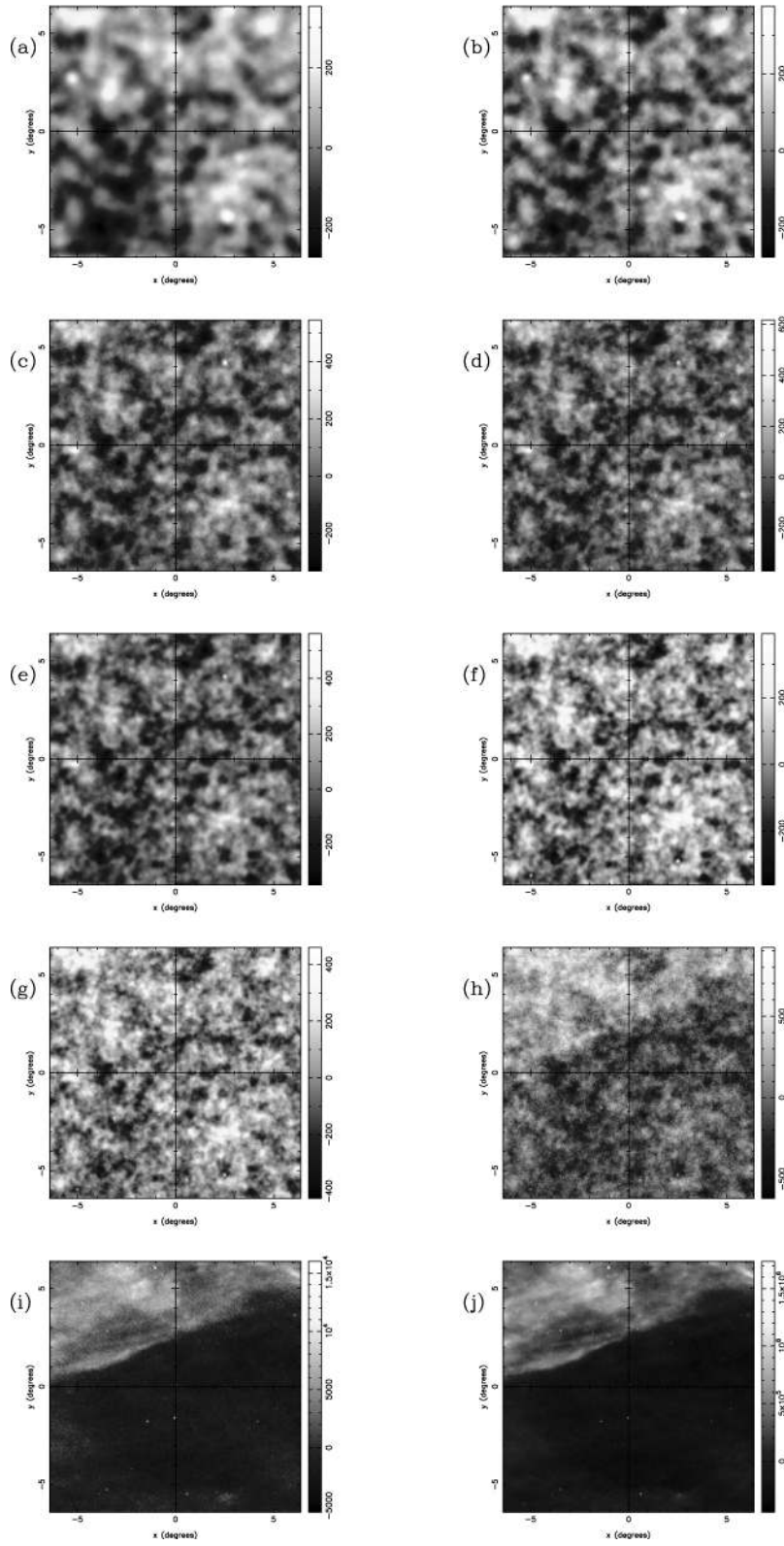
[1] http://www.swarthmore.edu/Home/News/Astronomy/

[2] http://www.astro.wisc.edu/wham/

**Figure 3.** The $12.8 \times 12.8 \, \mathrm{deg}^2$ data maps observed at each of the ten *Planck* frequency channels listed in Table 2. The panels correspond to the frequencies: (a) 30 GHz, (b) 44 GHz, (c) 70 GHz, (d) 100 GHz-lfi, (e) 100 GHz-hfi, (f) 143 GHz, (g) 217 GHz, (h) 353 GHz, (i) 545 GHz and (j) 857 GHz. The units are equivalent thermodynamic temperature in μK.
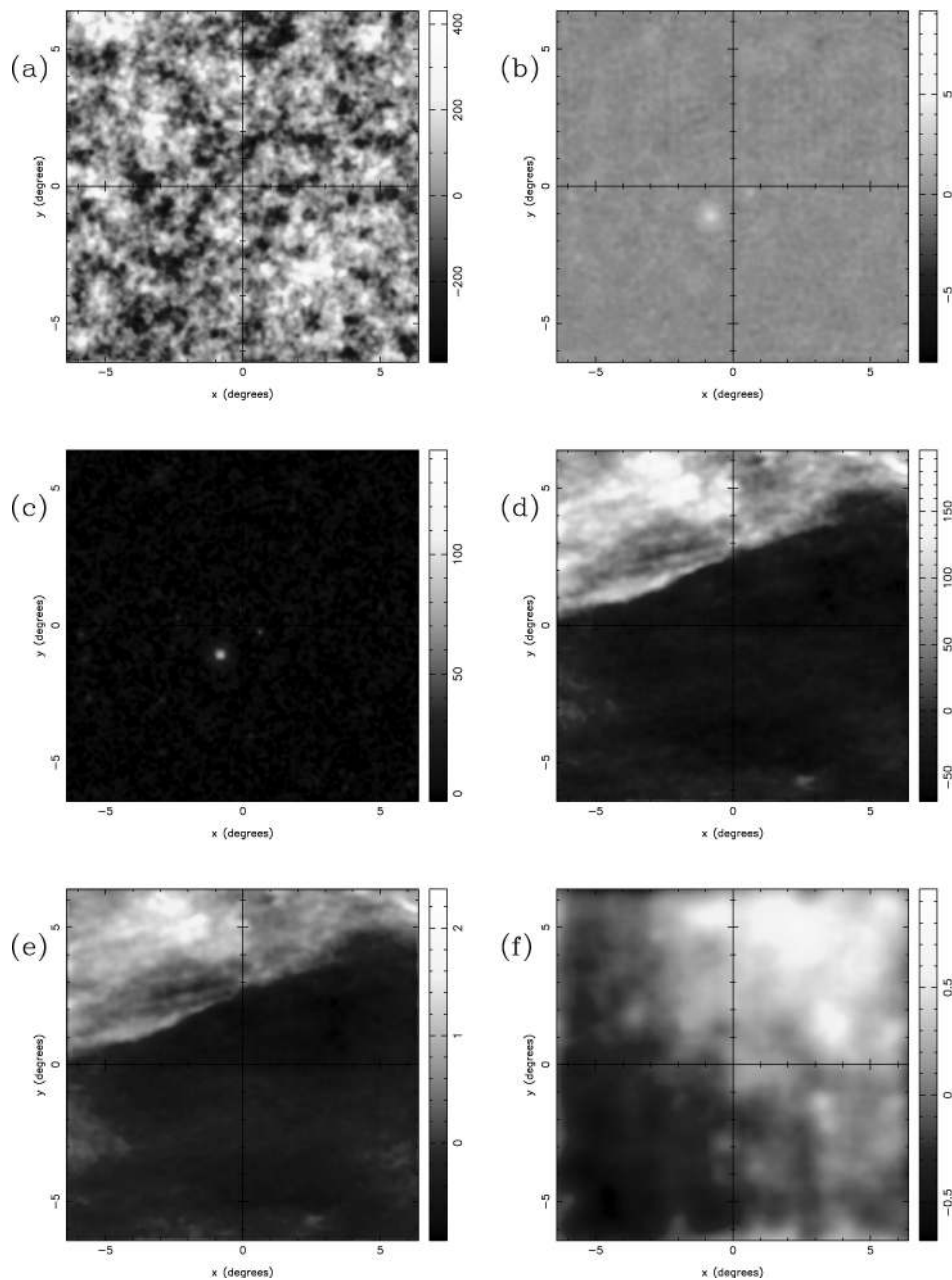
**Figure 4.** The reconstructed maps for each of the physical components: (a) CMB, (b) kinetic SZ effect, (c) thermal SZ effect, (d) Galactic dust, (e) Galactic free−free and (f) Galactic synchrotron emission. Point sources have been subtracted from the data maps using the Mexican hat algorithm before applying MEM. Each component is plotted at 300 GHz and has been convolved with a Gaussian beam of FWHM 5 arcmin. The map units are equivalent thermodynamic temperature in μK.

in the manner proposed by Bouchet, Gispert & Puget (1996). The frequency dependence of the free−free emission is assumed to vary as $I_\nu \propto \nu^{-0.16}$, and is normalized to give an rms temperature fluctuation of 6.2 μK at 53 GHz. Finally, the synchrotron spatial template has been produced using the all-sky map of Fosalba & Giardino[3]. This map is an extrapolation of the 408-MHz radio map of Haslam et al. (1982), from the original 1-deg resolution to a resolution of about 5 arcmin. The additional small-scale structure is assumed to have a power-law power spectrum with an exponent of −3. We have continued this extrapolation to 1.5 arcmin following

the same power law. The frequency dependence is assumed to be $I_\nu \propto \nu^{-0.9}$ and is normalized to the Haslam 408-MHz map.

To simulate the observed data in a given *Planck* frequency channel, each of the physical components discussed above is first projected to the relevant frequency and the contributions are summed. The predicted point-source emission for the frequency is then added, and the resulting total sky emission is convolved with a Gaussian beam of the appropriate FWHM. Finally, independent pixel noise is added, with corresponding rms from Table 2. In Fig. 2 we give the rms thermodynamic temperature fluctuations in the data at each *Planck* observing frequency due to each physical component and the instrumental noise. In Fig. 3 we plot the simulated *Planck* observations in each frequency channel, all the
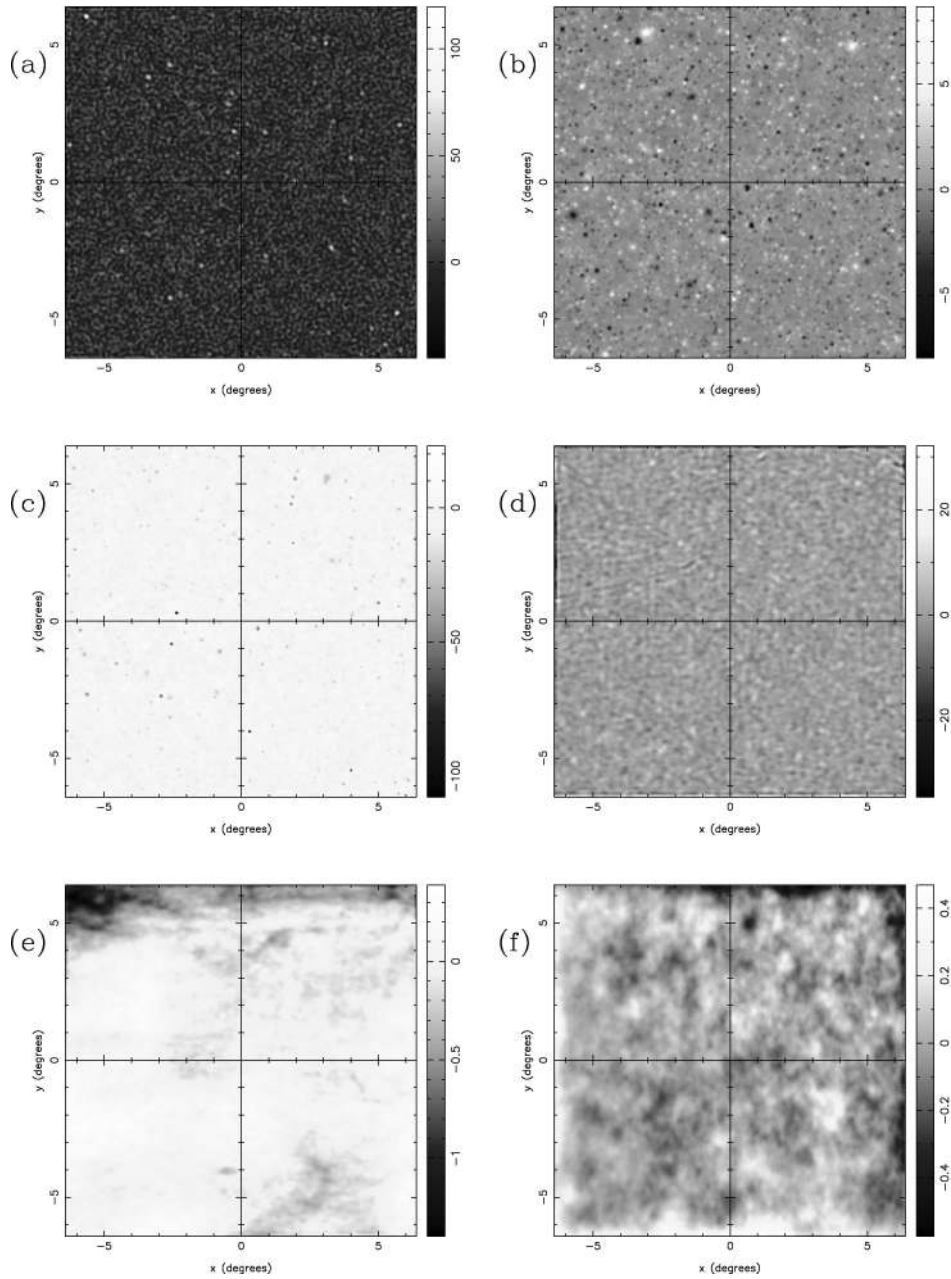
[3] ftp://astro.estec.esa.nl/pub/synchrotron

**Figure 5.** The reconstruction residuals obtained from subtracting the input maps of Fig. 1 from the reconstructed maps of Fig. 4. The panels correspond to: (a) CMB, (b) kinetic SZ effect, (c) thermal SZ effect, (d) Galactic dust, (e) Galactic free−free, (f) Galactic syncrotron emission.

components are included: CMB, dust, free−free, synchrotron, kinetic and thermal SZ effects and point-source emission as well as instrumental noise.

## 4 FOREGROUND SEPARATION

We have applied the method outlined in Section 2.3 to the simulated *Planck* data described above. We have assumed knowledge of the azimuthally averaged power spectra of the six input components in Fig. 1, together with the azimuthally averaged cross power spectra between them (see H98 for more details). Using the model of Toffolatti et al. (1998), we have also introduced the power spectrum of the point sources at each frequency channel, including cross power spectra between channels, and account for

this contaminant as an extra noise term (see H99 for more details). However, the recovery of the main components and point sources does not depend critically on this assumption, as will be discussed later.

The resulting reconstructions of the physical components at a reference frequency of 300 GHz are shown in Fig. 4. The maps have been plotted using the same grey-scale as in Fig. 1 to allow a straightforward comparison. In Fig. 5, we plot the residuals for each component, obtained by subtracting the input maps from the reconstructions.

We can see that the main input components have been faithfully recovered with no obvious visible contamination from point sources. This is because the MHW subtraction algorithm is efficient at removing the brightest point sources, whereas MEM

**Table 3.** The rms in $\mu$K of the reconstruction residuals smoothed with a 5-arcmin FWHM Gaussian beam with and without the initial subtraction of bright point sources using the MHW. Full power spectrum information has been assumed. For comparison, the rms of the input maps shown in Fig. 1 are also given. Results are given for the reference frequency 300 GHz.

| Component | Input rms | Error (with MHW) | Error (without MHW) |
|---|---|---|---|
| CMB | 112.3 | 7.68 | 8.62 |
| Kinetic SZ | 0.69 | 0.70 | 0.70 |
| Thermal SZ | 5.37 | 4.64 | 4.66 |
| Dust | 55.8 | 2.68 | 3.39 |
| Free−free | 0.66 | 0.22 | 0.24 |
| Synchrotron | 0.32 | 0.11 | 0.12 |

has greatly reduced the contamination due to fainter sources. We give the rms reconstruction errors for each component in Table 3.

In particular, we note that the CMB has been recovered very accurately, although the residuals map does show some weak contamination due to low-amplitude point sources. Indeed, the rms reconstruction error for this component is ∼7.7 μK, which corresponds to an accuracy of ∼6.8 per cent as compared with the rms of the input CMB map (see Table 3). Even more impressive is the reconstruction of the dust map. None of the numerous point sources present in the highest frequency channel maps are visible in the reconstruction. This is also confirmed by inspecting the residual map. The main features of the free−free emission are also recovered, mostly owing to its high correlation with the dust. Again, the reconstruction shows no evidence of point-source contamination. For the synchrotron component, the recovered emission is basically a lower resolution image of the input map. This is expected since only the lowest frequency channels provide useful information about this component, and these channels also have the lowest angular resolutions. Although the reconstructed synchrotron map is mostly free of point sources, some residual contamination remains. This contamination corresponds to a few medium-amplitude point sources that are present in the lowest frequency channels, although they are not clearly visible in the data. These sources are too weak to be detected using the MHW algorithm but at the same time they are not well characterized by the generalized noise approach assumed in MEM.

As pointed out in H99, one must be careful when comparing the amplitude of the residual point sources still contaminating the reconstructions with the corresponding amplitudes of the point sources in the data maps. The reconstructions are calculated at a reference frequency of 300 GHz and those sources remaining in the residuals maps are projected in frequency according to the spectral dependence of the component they contaminate. In addition, we have to take into account the different resolution of the *Planck* frequency channels. For example, the contaminating point source in the middle right-hand side of the synchrotron residuals map has an amplitude of $\simeq 0.15\,\mu$K after convolution with a Gaussian beam of FWHM 33 arcmin (the resolution of the 30-GHz *Planck* frequency channel). Following the spectral dependence of the synchrotron component, this projects to 17.5 μK at 30 GHz. This value should be compared with the amplitude of the point source at the same frequency, which is around 150 μK. Therefore, MEM has succeeded in reducing the contamination due to this point source by almost a factor of ten.

The recovery of the thermal SZ effect is quite good. Most of the

bright clusters have been reproduced whereas only a few point sources have been misidentified as clusters. At the reference frequency of 300 GHz, these misidentified point sources appear mostly as negative features. Finally, as expected, the reconstruction of the kinetic SZ is quite poor and one detects only a few clusters whose corresponding thermal SZ effect is large.

We have also calculated the power spectrum of the reconstructed component maps and found that the accuracy is very similar to that found in H99, so we do not plot them again here. The effect of first applying the MHW to the data maps before the MEM analysis is not so obvious when considering the power spectra of the reconstructions, since only a small percentage of pixels are affected by residual point sources and this has little effect in the recovered spectrum. Nevertheless, the removal of the point-source contamination is vital if one wishes to probe the Gaussian character of the CMB, as well as to study properties of the other foreground components.

To understand better the effect of performing the MHW analysis on the data maps prior to the MEM algorithm, we have also carried out a component separation for the case where the MHW step is *not* performed; this corresponds to the method in H99. In Fig. 6, we show the difference between the reconstructions obtained using the combined MHW/MEM technique and those obtained using MEM alone. Thus these maps display the point sources that have been successfully removed by the MHW, which would otherwise be present in the reconstructions. By comparing with the data, we can also see how the point sources present in the different frequency channels would affect a given component if not carefully subtracted. Particularly impressive is the removal from the dust and free−free reconstructions of the large number of point sources that were present in high-frequency data channels. For the CMB, the MHW has subtracted a few very bright point sources, which dominated the contribution of this contaminant in the intermediate frequency channels. We also note that the MHW has removed a few from the synchrotron reconstruction that were present in the lowest channels. The reconstructions of the thermal and kinetic SZ effects have also been improved since a lower number of point sources have been misidentified as clusters; these sources were detected by the MHW mainly in the highest channels of the LFI. The rms reconstructions errors when MEM is used without a previous subtraction of point sources by the MHW are also given in Table 3.

Finally, we can also study how our reconstructions are affected if we do not assume full power spectrum information. Thus, we have repeated our joint analysis of the simulated *Planck* observations for the case where we assume that $\ell^2 C_\ell$ is constant for each component out to the highest measured Fourier mode. The level of the flat power spectrum for each component is, however, chosen so that the total power in each component is approximately that observed in the input maps in Fig. 1. Furthermore, no information about the cross power spectra between different components is given. Regarding the point sources, the true azimuthally averaged power spectrum is again assumed to account for their contribution as an extra noise term but cross-correlations between different frequency channels are ignored. The quality of the reconstructions of the main components is actually very similar to the case when full power spectrum information is given. In particular, the accuracy of the CMB reconstructed map is only slightly worse with an rms error of 8.2 μK as compared with 7.7 μK in the former case. Moreover, the reconstruction is again free from obvious contamination due to point sources. Similarly, the dust component has been faithfully recovered with a rms error of 3.0 μK versus
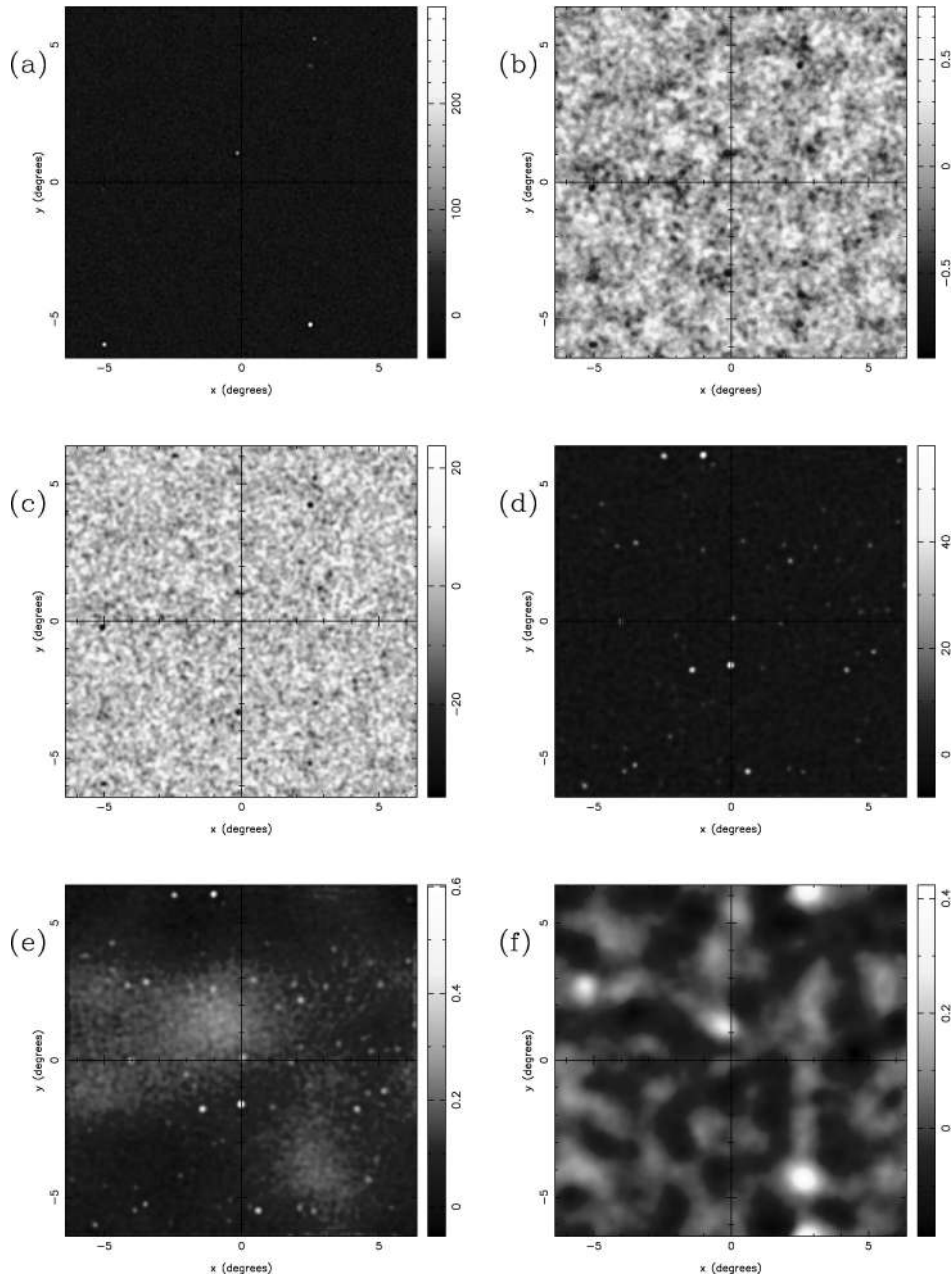
**Figure 6.** The residuals obtained by subtracting the reconstructed maps shown in Fig. 4 from the reconstructions achieved when the MHW is not used to perform an initial point-source removal. Both reconstructions were smoothed with a Gaussian beam of FWHM 5 arcmin and correspond to a frequency of 300 GHz. The different panels are: (a) CMB, (b) kinetic SZ effect, (c) thermal SZ effect, (d) Galactic dust, (e) Galactic free–free and (f) Galactic synchrotron emission. The map units are equivalent thermodynamic temperature in μK.

2.7 μK when full power spectrum is assumed. The main features of the synchrotron and thermal SZ effect are also recovered, although the reconstructions are poorer. In particular, the contamination due to point sources is slightly increased in the thermal SZ reconstructed map. Finally, the weakest components, free–free emission and kinetic SZ effect, are lost in this case and the reconstructions have simply defaulted to zero in the absence of any useful information.

## 5 RECOVERY OF POINT SOURCES

The previous section focused on the recovery of the six physical

component maps shown in Fig. 1. However, a major aim of the *Planck* mission is also to compile point-source catalogues at each of its observing frequencies. In this section, we compare the catalogues obtained using MEM alone (i.e., without a previous subtraction of bright sources detected by the MHW), MHW alone and the joint analysis method M&M.

The MHW catalogue (MHWc) is produced in the manner explained in V01, through the so called 50 per cent error criterion (see the previous work for more details in detection criteria). In short, each of the data maps of Fig. 3 is independently analysed with the MHW. Those coefficients above $2\sigma_{w_d}$ at the optimal wavelet scale are identified as point-source candidates. A

multiscale fit is then performed in order to estimate their amplitude and those wavelet coefficients with a non-acceptable fit are discarded. We then look for the flux above which at least 95 per cent of the detected point sources have a relative error ≤50 per cent. This gives our estimation of the flux limit. Thus, the number of detections at a given channel is given by those point sources with an estimated amplitude above the flux limit. In practice, we also use multifrequency information to include those point sources that, having an error larger than 50 per cent or an insufficiently good fit, have been detected in an adjacent channel (although in most channels this only accounts for a very small fraction of the detected point sources). The error is defined as: $E = |A - A^e|/A$, where $A$ is the flux of the simulated source and $A^e$ that of the estimated one.

Although the MHW catalogue (hereafter MHWc) is obtained in the same way as that of V01, the results here differ slightly. This apparent discrepancy is due to the different sampling rates that have been considered in each case. V01 assumes pixel sizes of 1.5, 3 and 6 arcmin for the different *Planck* channels, whereas in this work the pixel size is given by a fixed sampling of 2.4, following by a regridding to pixels of size 1.5 arcmin. Therefore, the number of detected point sources and fluxes of V01 and this paper are not directly comparable.

Nevertheless, not all the point sources in the MHWc are subtracted from the original maps prior to performing the MEM analysis. In theory, giving as much information as available should improve the MEM results. However, when using the 50 per cent error criterion a significant number of point sources, especially at the 545 and 857 GHz channels, are estimated with a large error. Therefore, if this information is given to MEM (by subtracting these sources from the original maps), we are misleading the MEM algorithm. To avoid this unwanted effect, the point sources subtracted from the maps should be those with the lowest errors in the amplitude estimation. We need a more robust criterion than that of the 50 per cent error. Instead we adopt the so-called $5\sigma_{w_d}$ criterion, which is also explained in V01. Briefly, we consider that a point source has been detected if the position of its maximum is above $5\sigma_{w_d}$ and its multiscale fit is acceptable.

The MEM catalogue (MEMc) and the M&M one (M&Mc) are obtained using the method outlined in H99. First, the reconstructed maps of Fig. 4 are used as inputs to produce 'mock' data. We follow the same procedure as that used to obtain the data of Fig. 3 but, of course, we do not add instrumental noise or the point sources. These mock data are then subtracted from the true data (which contain the full point-source contribution). Since the reconstructions of the six main components are reasonably accurate and also contain very few point sources, we obtain a data residuals map at each *Planck* frequency that consists mainly of the point sources and instrumental noise. Each of these residuals maps are then independently analysed in order to produce a point source catalogue at each observing frequency. We point out, however, that the residuals maps produced here differ from those in H99. In order to concentrate on the effect of emission from other physical components on the point-source recovery, in H99 the instrumental noise was neglected when making the residuals maps. Here the instrumental noise is included to obtain a more realistic estimate of the number of point sources recoverable from real *Planck* data.

Another difference with H99 is the process by which the point-source catalogue is produced from the residuals maps. In H99, the SExtractor package (Bertin & Arnouts, 1996) is used to detect and estimate the amplitude of point sources. The SExtractor package begins by fitting and subtracting an unresolved background

component, before identifying any point sources, and can lead to ambiguities in assigning a flux detection limit. Therefore, in the present paper, the residuals maps are instead analysed using the MHW, since this wavelet filter is optimal for this purpose (Sanz et al. 2000). At this point, however, it is worth pointing out some subtleties associated with applying the MHW in these circumstances. In particular, for the MEMc and M&Mc, we apply the 50 per cent error criterion into the residual maps, in order to compare with the MHWc. Clearly, this choice determines empirically the flux limit of the catalogue (achieved by the 50 per cent error criterion) and will depend on the assumed point-source population model, but we expect that most models lead to similar results. In fact, in V01 it is shown that for the Guiderdoni et al. (1998) E model, the flux limits achieved are very similar.

In Table 1 we give, for each catalogue, the number of point sources detected, the minimum flux achieved and the average amplitude error in each *Planck* frequency channel.

In the two highest frequency channels, the joint analysis clearly outperforms the results obtained with each of the methods separately. This is due to the complementary nature of the two approaches, so that bright sources are detected by MHW and intermediate flux sources are identified by MEM. If MEM alone is used, many of the brightest point sources remain in the MEM reconstructions since they are not well characterized by a generalized noise. Therefore they are either not detected in the data residuals maps or the error in the estimated amplitude is significantly large. However, in the joint analysis these sources are easily detected and their fluxes accurately estimated.

Regarding the 353-GHz channel, the number of point sources detected with M&M is comparable with the best of the individual methods, i.e. when using MEM on its own. This is due to the fact that the main contaminant of the residuals maps is the high level of noise of the 353-GHz channel, which is equally present in both the residuals obtained with MEM and with M&M. In fact, many of the point sources have been detected (with a large error) thanks to the multifrequency information.

The low number of point sources detected at intermediate frequencies (217 and 143 GHz) in the M&Mc in comparison with the MHWc can be explained as a combination of factors. First of all, owing to the high level of noise in these channels relative to the point-source emission, only a few point sources are detected with the MHW in the first step of our analysis, through the $5\sigma_{w_d}$ criterion. Therefore, when applying MEM, part of the emission of the undetected point sources is left in the reconstructed components, being mainly misidentified with CMB, which is the dominant component at those frequencies. This has the effect of lowering the level of the point sources in the data residuals, which together with the high level of noise, leads to a low number of recovered point sources.

In the low-frequency channels, the number of point sources detected by the joint analysis is similar to that by MEM alone (the fact that M&M does not work better than MEM alone for all the channels may be understood as a statistical fluctuation; we expect that with an all-sky point-source simulation, the results of the combined method will be better than those of MEM in every case). In this case, the MHW contribution is to improve the amplitude estimation of a few point sources, which leads to a lower average amplitude error. In these frequency channels, MHW alone detects only the few brightest point sources. This is because these channels are dominated by the CMB and the beam FWHM is so large that the CMB and point sources have a similar characteristic scale.
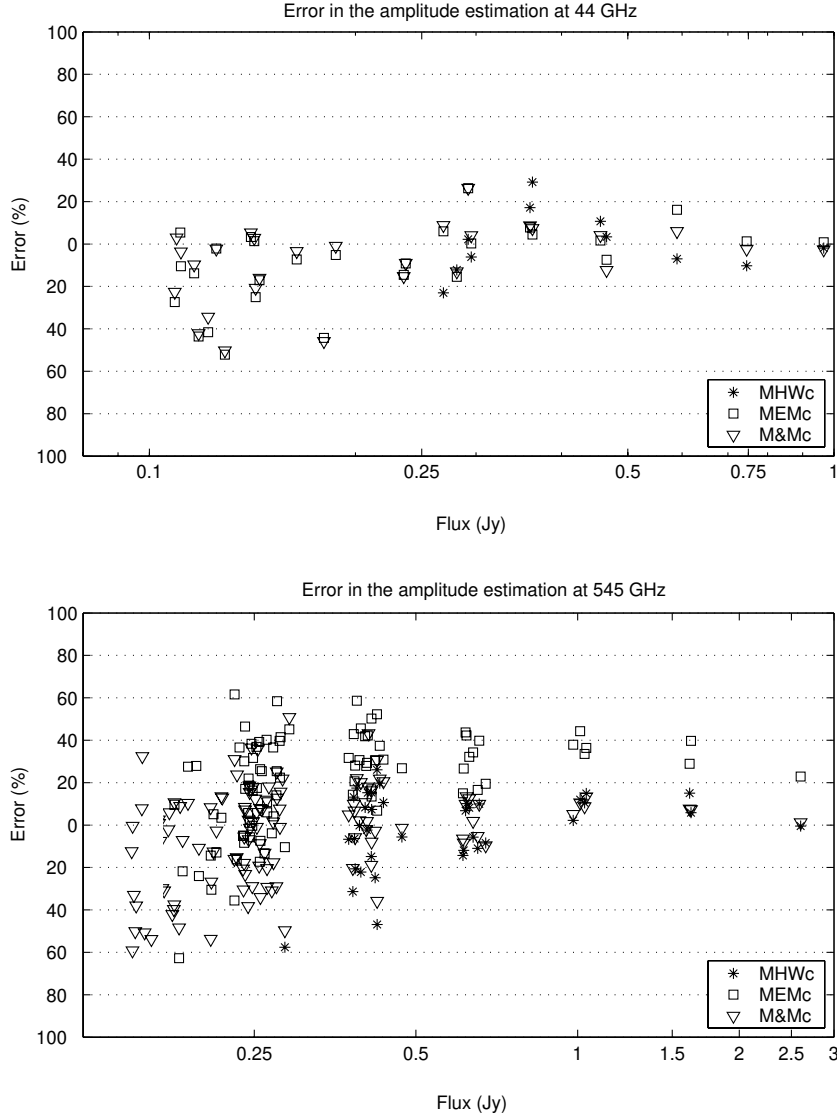
Error in the amplitude estimation at 44 GHz



Error in the amplitude estimation at 545 GHz



**Figure 7.** Errors in the amplitude estimation for the MHW, MEM and joint analysis catalogues (MHWc, MEMc and M&Mc, respectively) as a function of the flux. We plot two *Planck* frequencies: 44 GHz (top) and 545 GHz (bottom).

Regarding the estimation of point-source amplitudes, the joint analysis also performs better than each method independently. Although the average error in the amplitude estimation can be larger in the M&Mc than in the MHWc owing to the detection of a larger number of faint point sources, those point sources present in all three catalogues are, on average, better estimated with the combined analysis.

In Fig. 7 we plot the amplitude estimation errors for the MHWc, MEMc and M&Mc versus the true flux (in Jy) for two representative channels: 44 and 545 GHz. We can see that there is a clear bias in the estimation of the amplitude of the brightest point sources in MEMc since they remain in the reconstructions and are therefore underestimated (corresponding to positive errors in Fig. 7). This problem is solved when combining MEM and the MHW. It is also obvious that a larger number of point sources and fainter fluxes are achieved in the combined analysis with respect to the MHW on its own.

In Fig. 8 we have plotted the sources in M&Mc, for the same two channels, together with the input point-sources maps. We

see that the main features are very well recovered. At 44 and 545 GHz, the flux limit is comparable with the level of instrumental noise (see the next section). Thus, to increase still further the number of point sources detected and reach fainter fluxes, one would need to denoise the residuals maps; this is discussed in the next section.

We have also investigated the effect of reducing the power spectrum information given to MEM. We find that even in the extreme case when a flat power spectrum is assumed for the different components, the results are not significantly different for the M&Mc, but the quality of the MEMc is somewhat reduced, especially in the high frequency channels. In particular, the amplitude estimation errors are higher and the catalogue flux limit increases slightly.

## 6 DISCUSSION AND CONCLUSIONS

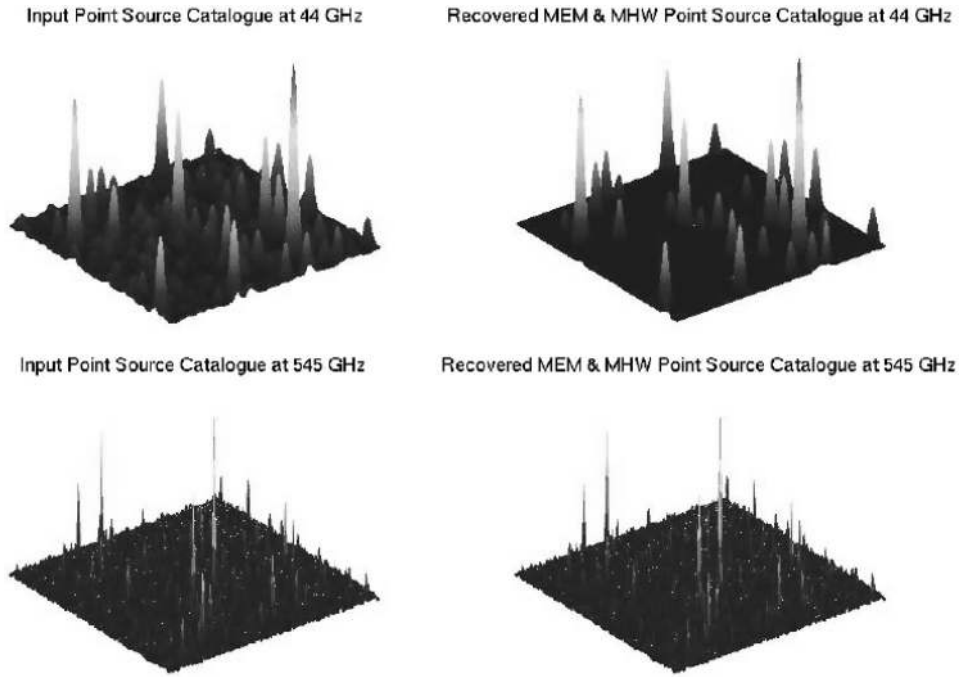The MEM (H98, H99) and the MHW (C00, V01) techniques have complementary characteristics when recovering the microwave

Input Point Source Catalogue at 44 GHz

Recovered MEM & MHW Point Source Catalogue at 44 GHz

Input Point Source Catalogue at 545 GHz

Recovered MEM & MHW Point Source Catalogue at 545 GHz

**Figure 8.** Input and recovered point-source catalogues for the 44-GHz (top) and 545-GHz (bottom) *Planck* channels. The catalogues are convolved with the corresponding *Planck* beams.

**Table 4.** M&M estimation of a two-thirds of the sphere point-source catalogue (see text for details).

| Frequency (GHz) | ∼ counts in M&Mc | ∼ counts in the model | Percentage |
|---|---|---|---|
| 30 | 5000 | 7500 | 66 |
| 44 | 4500 | 4500 | 75 |
| 70 | 5800 | 6800 | 85 |
| 100 (LFI) | 7000 | 10800 | 65 |
| 100 (HFI) | 12000 | 24300 | 49 |
| 143 | 800 | 900 | 89 |
| 217 | 800 | 850 | 94 |
| 353 | 6000 | 13000 | 46 |
| 545 | 20000 | 32000 | 63 |
| 857 | 82000 | 200000 | 41 |

sky. On the one hand, the MEM technique is a powerful tool for using multifrequency data to separate the cosmological signal from foreground emission whose spectral behaviours are (reasonably) well known. The most problematic foreground to remove is that due to point sources. On the other hand, the MHW has been shown to be a robust and self-consistent method for detecting and subtracting this point-source emission from microwave maps. The aim of this paper has been to show how the performance of a combined (MEM and MHW) analysis can improve the recovery of the components (CMB, Sunyaev–Zel'dovich, extragalactic point sources and Galactic emission) of simulated microwave maps. In order to test this analysis, we have applied it to simulated ESA *Planck satellite* observations. However, the technique could straightforwardly be applied to other CMB experiments (e.g. the NASA *MAP* satellite and the BOOMERANG and MAXIMA balloon experiments).

The proposed method for analysing these data is as follows. First, we apply the MHW at each observing frequency in order to remove the brightest point sources and obtain very good amplitude estimations. The MEM technique is then applied to these maps to reconstruct the different components (except the remaining point-sources contribution, which is treated as an additional 'noise'). Following the approach discussed in H99, we generate mock observed data from our reconstructions. These maps are then subtracted from the initial data. This provides data residuals maps that mostly contain instrumental noise plus point-source emission (with slight traces of unrecovered diffuse components). These residual maps are then analysed again with the MHW in order to refine the number of detections and the amplitude estimation of the point sources.

As already discussed in Section 4, the joint analysis improves the accuracy of the component separation of all the diffuse components. This is so because the MHW subtraction algorithm is efficient at removing the brightest point sources, whereas MEM has greatly reduced the contamination due to fainter sources. We compare the reconstructions achieved when the MHW is or is not applied. In particular, Fig. 6 shows how many point sources would remain in the reconstructed components if the MHW were not used. We can see that a large number of point sources are removed from the dust and free–free maps. There are also a handful of point sources that would contaminate the synchrotron emission coming from the low-frequency channels. A lower number of point sources would affect the CMB reconstruction since the cosmological signal is the main component at the intermediate *Planck* frequencies, where point-source emission is lower. Finally, a few point sources would be misidentified with SZ clusters, appearing in the reconstruction at the reference frequency as sharp negative features.

In the previous section, we gave estimates of the point-source catalogues that MEM, MHW and the joint method provide for these simulations (see Table 1). We see that the joint analysis provides, in general, a more complete catalogue than each of the methods on its own, reaching lower fluxes and with point-source

amplitude more accurately estimated. The improvement is especially clear at high frequencies owing to the high resolution of those *Planck* channels. The differences between the number of detections in the MEMc and M&Mc are smaller for the channels between 30 and 100 GHz. This is due to the difficulty of detecting point sources using the MHW when the background has a similar scale variation to that of the point sources (see V01 for more details). Hence the main contribution of the MHW at these frequencies is in improving the amplitude estimation. In Table 4 we give an estimate of the number of point sources that would be detected with this combined method in two-thirds of the sky after 12 months of observation with the *Planck* satellite. This number is simply obtained by multiplying the counts of Table 1 by the ratio between the solid angle covered by two-thirds of the sphere and that covered by our simulations. We compare the recovered point-source catalogue with the simulated one, with a cutoff as given by the 'Min Flux' column for M&M given in Table 1. We can see that for most of them, the percentage of detection is around or above 50 per cent. Current evolution models of dust emission in galaxies (see, e.g., Franceschini et al. 1994; Guiderdoni et al. 1998; Granato et al. 2000) give different predictions for counts in the high-frequency *Planck* channels. On the other hand, all these models predict a very sharp increase of the far−IR/sub−mm galaxy counts at fluxes $\simeq 20-100$ mJy. Therefore, given the detection limits of Table 1, *Planck* data alone will not be able to disentangle among different models, although it could marginally detect the sharp increase in the counts in the channels where the minimum flux achieved lies below 100 mJy. In any case, *Planck* will provide very useful data on counts, in a flux range not probed by other experiments. These data, complementary to the deeper surveys from the ground or from space (ESA *FIRST* and *ASTRO−F/IRIS* missions), will surely allow one to discriminate among the various evolutionary scenarios.

Spectral information about the point sources could also be used to improve further the recovered catalogues. Indeed, V01 have shown that following point sources through adjacent channels, one can estimate the spectral indices of the different point-source populations. This would allow the recovery of point sources that, albeit below the detection limit, have an amplitude and position in agreement with those predicted from adjacent channels.

Finally, as pointed out in the previous section, the flux limits achieved in the M&Mc are close to the noise level. Indeed, the faintest point sources detected in the catalogue have a fluxes which are 3.0, 2.4, 1.6, 1.2, 1.1, 11.2, 6.7, 1.1, 1.3 and 1.4 times the noise rms in the 30, 44, 70, 100(LFI), 100(HFI), 143, 217, 353, 545 and 857 GHz channels, respectively. To reach fainter fluxes in these channels is a difficult task, since we are very close to the noise level except for the 143 and 217 GHz channels. On the other hand, if we subtract the MHWc sources from the original data at 143 and 217 GHz, instead of the point sources detected by the $5\sigma_{w_d}$ criterion, we could greatly increase the number of sources and the depth of the M&Mc at those frequencies. A possibility to improve the results at all frequencies could be to denoise these data residual maps. One way is using wavelet techniques that have been proved to be very efficient at removing noise from CMB maps (Sanz et al. 1999a,b). However, care must be taken when denoising the residuals maps since the denoising procedure may change the profile of the point source in wavelet space. A detailed study of the properties of the denoised map would then become necessary. In this case, instead of the Mexican hat, one could use a customized pseudo-filter to detect point sources in the residuals maps as proposed by Sanz et al. (2000).

A natural way to improve the results is to subtract the recovered M&Mc from the original data and apply the MEM algorithm again. This process could be performed iteratively until the flux limits and the number of counts converge. However, this method has some disadvantages. As pointed out in the previous section, if the sources subtracted from the input maps have a large error, this could mislead the MEM algorithm. This is the reason we choose to subtract the catalogue achieved by the $5\sigma_{w_d}$ criterion instead of subtracting the one given by the 50 per cent error criterion. The number of point sources with *large errors* in the M&Mc is larger than in the MHWc obtained with the 50 per cent error criterion. Hence, a more detailed analysis becomes necessary in order to improve the results with an iterative approach. Such a study will be performed in a future work, where the combined technique will be extended to the sphere. Moreover, the flux limits are already close to the noise level and thus we do not expect the detection levels to change substantially (except for the 143- and 217-GHz channel, which can be clearly improved).

## REFERENCES

Baccigalupi C. et al., 2000, MNRAS, 318, 769
Balbi A. et al., 2000, ApJ, 545, 1
Bennet C. et al., 1996, Amer. Astro. Soc. Meet., 8805
Bertin E., Arnouts S., 1996, A&AS, 117, 393
Bouchet F. R., Gispert R., Puget J. L., 1996, in Drew E. ed., Proc. AIP Conf. 384, The mm/Sub-mm Foregrounds and Future CMB Space Missions. AIP Press, New York, p. 255
Cayón L. et al., 2000, MNRAS, 315, 757 (C00)
de Bernardis P. et al., 2000, Nat, 404, 955
Diego J. M., Martínez-González E., Sanz J. L., Cayón L., Silk J., 2001, MNRAS, 325, 1533
Finkbeiner D. P., Davis M., Schlegel D. J., 1999, ApJ, 524, 867
Franceschini A., Mazzei P., De Zotti G., Danese L., 1994, ApJ, 427, 140
Granato G. L., Lacey C. G., Silva L., Bressan A., Baugh C. M., Cole S., Frenk C. S., 2000, ApJ, 542, 710
Guiderdoni B., Hivon E., Bouchet F. R., Maffei B., 1998, MNRAS, 295, 877
Haslam C. G. T., Salter C. J., Stoffel H., Wilson W. E., 1982, A&AS, 47, 1
Hobson M. P., Jones A. W., Lasenby A. N., Bouchet F. R., 1998, MNRAS, 300, 1 (H98)
Hobson M. P., Barreiro R. B., Toffolatti L., Lasenby A. N., Sanz J. L., Jones A. W., Bouchet F. R., 1999, MNRAS, 306, 232 (H99)
Mandolesi N. et al., 1998, Proposal submitted to ESA for the *Planck* Low Frequency Instrument
Press P. H., Teukolsky S. A., Vettering W. T., Flannery B. P., 1994, Numerical Recipes. Cambridge Univ. Press
Puget J. L. et al., 1998, Proposal submitted to ESA for the *Planck* High Frequency Instrument
Sanz J. L., Argüeso F., Cayón L., Martínez-González E., Barreiro R. B., Toffolatti L., 1999a, MNRAS, 309, 672

Sanz J. L. et al., 1999b, A&AS, 140, 99

Sanz J. L., Herranz D., Martínez-González E., 2000, ApJ, 552, 484

Seljak U., Zaldarriaga M., 1996, ApJ, 469, 437

Tegmark M., Oliveira-Costa A., 1998, ApJ, 500, 83 (TOC98)

Tenorio L., Jaffe A. H., Hanany S., Lineweaver C. H., 1999, MNRAS, 310, 823

Toffolatti L., Argüeso F., De Zoti G., Mazzei P., Franceschini A., Danese L., Burigana C., 1998, MNRAS, 297, 117

Vielva P., Martínez-González E., Cayón L., Diego J. M., Sanz J. L., Toffolatti L., 2001, MNRAS, 326, 181 (V01)

This paper has been typeset from a TEX/LATEX file prepared by the author.